




Article

Gold Nanocluster-Based Fluorometric Banoxantrone Assay Enabled by Photoinduced Electron Transfer

Kai-Yuan Huang^{1,†}, Wen-Hui Weng^{1,2,†}, Xin Huang¹, Hong-Xiang Huang¹, Hamada A. A. Noreldeen¹, Hao-Hua Deng^{1,*} and Wei Chen^{1,*}

¹ Fujian Key Laboratory of Drug Target Discovery and Structural and Functional Research, School of Pharmacy, Fujian Medical University, Fuzhou 350004, China; 15980269577@163.com (K.-Y.H.); www18344910886@163.com (W.-H.W.); xinhuang5649@163.com (X.H.); hhx1830400660@163.com (H.-X.H.); haali8651@gmail.com (H.A.A.N.)

² Department of Pharmacy, Fujian Provincial Hospital, Fuzhou 350001, China

* Correspondence: hhdeng@fjmu.edu.cn (H.-H.D.); chenandhu@163.com (W.C.)

† These authors contributed equally to this work.

Abstract: Monitoring the blood concentration of banoxantrone (AQ4N) is important to evaluate the therapeutic efficacy and side effects of this new anticancer prodrug during its clinical applications. Herein, we report a fluorescence method for AQ4N detection through the modulation of the molecule-like photoinduced electron transfer (PET) behavior of gold nanoclusters (AuNCs). AQ4N can electrostatically bind to the surface of carboxylated chitosan (CC) and dithiothreitol (DTT) co-stabilized AuNCs and quench their fluorescence via a Coulomb interaction-accelerated PET process. Under optimized experimental conditions, the linear range of AQ4N is from 25 to 200 nM and the limit of detection is as low as 5 nM. In addition, this assay is confirmed to be reliable based on its successful use in AQ4N determination in mouse plasma samples. This work offers an effective strategy for AQ4N sensing based on fluorescent AuNCs and widens the application of AuNCs in clinical diagnosis and pharmaceutical analysis.

Keywords: gold nanocluster; banoxantrone; photoinduced electron transfer; photoluminescence quenching; Coulomb interaction



Citation: Huang, K.-Y.; Weng, W.-H.; Huang, X.; Huang, H.-X.; Noreldeen, H.A.A.; Deng, H.-H.; Chen, W. Gold Nanocluster-Based Fluorometric Banoxantrone Assay Enabled by Photoinduced Electron Transfer. *Nanomaterials* **2022**, *12*, 1861. <https://doi.org/10.3390/nano12111861>

Academic Editor: Raphaël Schneider

Received: 23 April 2022

Accepted: 25 May 2022

Published: 30 May 2022

Publisher's Note: MDPI stays neutral with regard to jurisdictional claims in published maps and institutional affiliations.



Copyright: © 2022 by the authors. Licensee MDPI, Basel, Switzerland. This article is an open access article distributed under the terms and conditions of the Creative Commons Attribution (CC BY) license (<https://creativecommons.org/licenses/by/4.0/>).

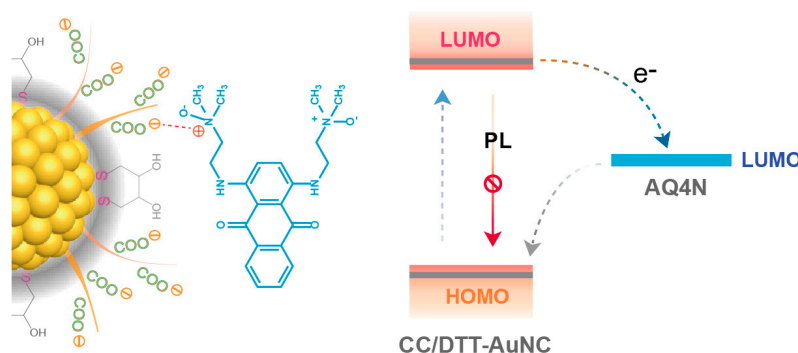
1. Introduction

Banoxantrone (AQ4N) is a novel hypoxia-activated prodrug that exhibits anticancer activity following bioreduction by heme-containing reductases to AQ4, an effective DNA intercalator and topoisomerase II inhibitor [1]. Although preclinical trials have revealed that AQ4N is relatively nontoxic in tumor treatments, the overdose use of AQ4N still faces the risk of severe side effects including cardiotoxicity and myelosuppression [2–4]. Consequently, the development of methods for precise monitoring and quantification of the blood concentration of AQ4N is of great significance. So far, high-performance liquid chromatography (HPLC) [5] and mass spectrometry (MS) [6] have been utilized for the detection of AQ4N. However, these approaches may suffer from some drawbacks such as time consumption and the involvement of toxic solvents. Therefore, it is greatly welcomed to establish rapid, accurate, and sensitive analytical techniques for measuring AQ4N concentration.

Photoinduced electron transfer (PET), where an excited electron transfers from an electron donor to an electron acceptor, is one of most popular mechanisms in the design of fluorescence-sensing strategies [7,8]. The PET process can happen within several picoseconds, which will quickly deactivate the emission-excited state of fluorophores and finally cause fast and remarkable luminescence quenching [9,10]. According to a classical theory, the dynamics of PET can be easily regulated by the excited-state parameters of electron transfer reactants including driving force (ΔG), reorganization energy (λ), and electron

coupling factor (HDA) [11]. Such features make PET an efficient technique to construct powerful chemo/biosensors for fluorescence detection of DNA [12,13], proteins [14,15], small biomolecules [16,17], drugs [18,19], ions [20,21], and so forth.

Ultrasmall gold nanoparticles (commonly known as gold nanoclusters, AuNCs) with a metallic core diameter less than 2 nm have become a new kind of fluorescent nanomaterial for developing PET sensors owing to their intriguing properties, such as long-wavelength photoluminescence (PL) and distinguishable electrochemical performance [22–27]. In a typical PET process of AuNCs, relatively weak electron–hole coupling will suppress Auger-assisted electron transfer behavior and thereby give rise to a distinguished Marcus inverted region [28–31]. Moreover, the fluorescence of a AuNC-based PET probe is sensitive to the alteration of their physicochemical characteristics, for instance, the surface charge, redox state, metallic core size, and ligand length [32–35]. Inspired by these attractive properties mentioned above, herein, a new fluorometric AQ4N assay was rationally designed by triggering molecule-like PET behavior of AuNCs (Scheme 1), in which the carboxylated chitosan (CC) and dithiothreitol (DTT) co-stabilized AuNCs (CC/DTT-AuNCs) served as an electron donor and AQ4N acted as an electron acceptor. Positively charged AQ4N can attach to the negatively charged CC/DTT-AuNCs. After that, AQ4N accepts an electron from the photoexcited CC/DTT-AuNCs and suppresses the PL as a result. The PET process between AQ4N and CC/DTT-AuNCs was systematically investigated and was solidly supported by experimental and calculation results. Furthermore, the proposed method was also applied to monitor AQ4N concentration in mouse plasma with satisfactory results.



Scheme 1. Illustration of the design principle of this AQ4N sensing strategy.

2. Materials and Methods

2.1. Chemicals and Reagents

AQ4N, $\text{HAuCl}_4 \cdot 3\text{H}_2\text{O}$, cisplatin (DDP), histidine (His), cyclophosphamide (CAR), L-cysteine (Cys), L-glutathione (GSH), ascorbic acid (AA), carboxylated chitosan (CC), dithiothreitol (DTT), bovine serum albumin (BSA), and N-acetyl-L-cysteine (NAC) were purchased from the Aladdin Reagent Co. (Shanghai, China) (<http://www.aladdin-e.com/>, accessed on 12 January 2022) Other analytical-grade chemicals were commercial and used directly without any further purification. Ultrapure water (>18 k Ω) was used throughout the experiments.

2.2. Preparation of CC/DTT-AuNCs

The AuNCs employed in this investigation were prepared and purified following our previously reported approach [30]. The optical properties of the resulting CC/DTT-AuNCs can be preserved without any change for at least three months at 4 °C in a refrigerator.

2.3. AQ4N Determination

AQ4N detection was performed using the following procedure: 0.1 mL of CC/DTT-AuNC solution was added to 1.9 mL of standard AQ4N solutions with different concentrations (in 20 mM phosphate buffer, pH 6.0). The emission spectra of the mixtures were monitored directly at an excitation wavelength of 290 nm.

2.4. AQ4N Extraction and Quantification

The extractions of AQ4N were carried out as follows: three adult mice each were given a dosage of 0.1 mL/g AQ4N solution (10 mM) by intraperitoneal injection. At the time point of 15 min, the whole blood was taken from orbits, placed into heparinized tubes on ice, centrifuged at 3000 rpm for 5 min, and then the separated plasma was collected. Finally, 100 μ L of the obtained plasma was mixed with 300 μ L of methanol followed by centrifugation at 7000 rpm for 8 min, and the supernatant was used in subsequent experiments.

Measurement of the AQ4N content in the extractions was performed by our developed method: 15 μ L of the supernatant and 0.1 mL of CC/DTT-AuNC solution were introduced into 1.885 mL phosphate buffer solution (20 mM, pH 6.0). Then, the emission spectra of resulting solutions were recorded immediately with an excitation wavelength of 290 nm.

Quantification of AQ4N concentration in the extractions by HPLC: A Shimadzu LC-15C (Shimadzu, Japan), equipped with an Agilent Zorbax SB-C18 column (5 μ m, 46 \times 250 mm i.d.) (Agilent Technology, Palo Alto, CA, USA) was operated at 25 $^{\circ}$ C. The separation conditions were: 1% formic acid solution containing 10 mM ammonium formate: acetonitrile, 75:25; a flow rate of 1 mL/min; and an injected volume of 20 μ L for the supernatant. A 245 nm SPD UV-Vis detector was used.

2.5. Computational Methodology

The luminescence quenching efficiency (E%) was determined using the following equation:

$$E\% = \left(1 - \frac{F}{F_0}\right) \times 100\% \quad (1)$$

where F_0 and F are luminescence intensities of CC/DTT-AuNCs at 645 nm in the absence and presence of AQ4N, respectively.

The inner filter effect (IFE) was corrected by the following equation [36]:

$$CF = \frac{F_{\text{cor}}}{F_{\text{obsd}}} = \frac{2.3dA_{\text{ex}}}{1 - 10^{-dA_{\text{ex}}}} 10^{gA_{\text{em}}} \frac{2.3sA_{\text{em}}}{1 - 10^{-sA_{\text{em}}}} \quad (2)$$

where F_{obsd} is the PL intensity of CC/DTT-AuNCs at 645 nm and F_{cor} is the corrected PL intensity obtained by removal of the IFE from F_{obsd} , while A_{ex} and A_{em} are the absorbances recorded at 290 nm (excitation wavelength) and 645 nm (emission wavelength), respectively. s , d , g are instrument-related geometrical parameters that are usually fixed at 0.1, 0.4, and 1.0 cm, respectively. CF represents a believable correction factor, which should not exceed 3.

The driving force was calculated by the Rehm–Weller equation [37]:

$$\Delta G = e \left(E_{\text{ox}}^{\text{D}} - E_{\text{red}}^{\text{A}} \right) - E_{0,0} + C \quad (3)$$

where E_{ox}^{D} (1.24 V, Figure S1) and $E_{0,0}$ (2.65 eV) are the first oxidation potential and 0–0 singlet–singlet excitation energy of CC/DTT-AuNCs, respectively; $E_{\text{red}}^{\text{A}}$ is the first reduction potential of AQ4N (−0.68V, Figure S2); and C represents the solvent-dependent Coulombic interaction energy, which is commonly ignored in water.

2.6. Instruments

Optical absorption spectra were conducted on a Shimadzu UV-2450 spectrophotometer (Shimadzu, Japan). A Cary Eclipse fluorescence spectrophotometer (Agilent, Palo Alto, CA, USA) was used to measure the fluorescence spectra. The transmission electron microscopy (TEM) image on a JEM-2100 microscope (JEOL, Tokyo, Japan) was employed to characterize the shape and size of CC/DTT-AuNCs. An F900 microsecond time-correlated single-photon-counting (TSPC) fluorescence lifetime spectrometer (Edinburgh Analytical Instruments, Edinburgh, UK) was used to determine the PL lifetime changes of CC/DTT-AuNC solutions in the absence and presence of AQ4N. The first redox potentials of the PET reactants were measured in a three-electrode system (a platinum wire, a bare glassy carbon

electrode, and an Ag/AgCl electrode were used as counter electrode, working electrode, and reference electrode, respectively) performed on a CHI 660C electrochemical analyzer (CHI Instrument Inc., Austin, TX, USA).

3. Results and Discussion

3.1. Designing Strategy

To rationally construct the fluorescence AQ4N sensor, we first screened the potential AuNC nanoprobe in light of the PET theory and the physicochemical characteristics of AQ4N (which is an electron-deficient molecule with a positive surface charge [38]). The theoretical investigations have pointed out that a high quenching ratio of fluorescent PET sensors will appear when the driving force approaches the reorganization energy [11]. Additionally, a previous report has demonstrated that a long excited-state lifetime will be of benefit for improving the sensitivity of luminescent PET sensors [39]. Recently, it was also found that the Coulomb interaction of ground-state PET reactants is capable of promoting fluorescence quenching efficiency due to an accelerated diffusion rate [40]. Taken together with these principles, CC/DTT-AuNCs were selected as the fluorescent nanoprobe, owing to their molecule-like PET behavior, appropriate oxidation potential, long luminescence lifetime, and negative surface charge (Table S1) [30,31]. The obtained CC/DTT-AuNCs exhibited two weak single-electron transitions in their UV-vis absorption spectrum, rather than the surface plasmons observed in metallic-state gold nanoparticles (Figure S3). The 3D PL spectra analysis of these AuNCs showed that the excitation and emission bands were centered at 290 and 645 nm, respectively (Figure 1A). A transmission electron microscope (TEM) image revealed that the spherical CC/DTT-AuNC particles were well-dispersed with a mean diameter of about 2.0 nm (Figure 1B).

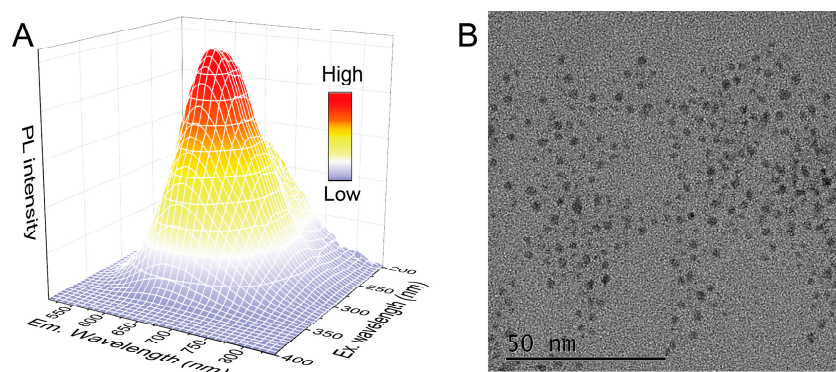


Figure 1. (A) Three-dimensional PL spectra of the prepared CC/DTT-AuNCs. (B) TEM image of CC/DTT-AuNCs.

3.2. Luminescence Quenching Mechanism Study

When an aqueous solution of AQ4N (1 μ M) was introduced into CC/DTT-AuNCs, a remarkable luminescence suppression was observed (Figure 2A). To better understand the luminescence quenching mechanism, a series of experiments were performed. IFE can be ruled out because the luminescence quenching efficiencies are almost identical before and after the removal of IFE by a correction formula (Figures S4 and S5, Table S2). Owing to the strong solvent-dependent quenching (Figure 2B), we can further safely exclude a Förster resonance energy transfer (FRET) mechanism since the appearance of FRET will not generate a polarity-sensitive electron transfer state [41]. Our previous works have demonstrated that the luminescence quenching in AuNC-cationic molecule assemblies is originated from a Coulomb interaction-accelerated PET process [30,31]. The possibility of this effect in the present system was then discussed. The Coulomb interaction between CC/DTT-AuNCs and AQ4N can be verified by the declined surface potential of CC/DTT-AuNCs after the addition of AQ4N (Figure 2C). By using the Rehm–Weller equation, the driving force of the AQ4N-CC/DTT-AuNCs PET system was calculated to be 0.74 eV,

which is close to the theoretical value of reorganization energy (0.67 eV, Table S1) and agrees well with the observed obvious luminescence quenching. Moreover, an apparent decrease in the average fluorescence lifetime of CC/DTT-AuNCs (from 8.9 to 1.7 μ s) upon the addition of AQ4N suggested that an additional nonradiative relaxation pathway is activated by the formation of an electron-transfer state (Figure 2D) [42,43]. These data firmly proved that the Coulomb interaction-accelerated PET is the dominant mechanism for the AQ4N-induced PL quenching of CC/DTT-AuNCs.

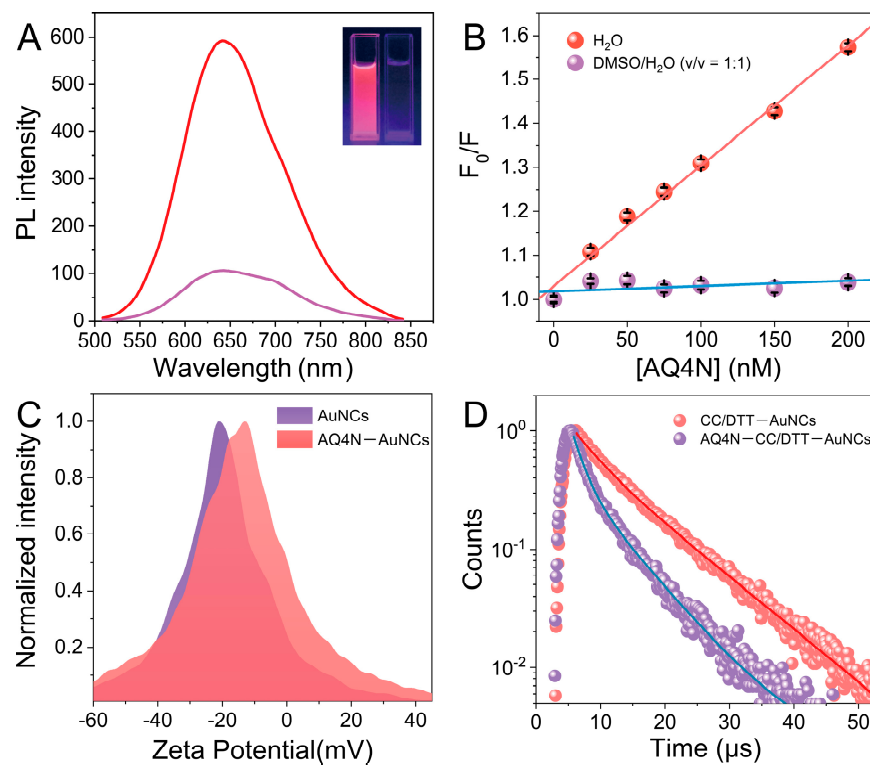


Figure 2. (A) The photoemission spectra of CC/DTT-AuNCs (red line) and CC/DTT-AuNCs + 1 μ M AQ4N (blue line). Inset shows the photographs of CC/DTT-AuNC solutions without (left) and with (right) the introduction of 1 μ M AQ4N under a 254 nm UV light. (B) The effect of solvent polarity on the luminescence suppression of AQ4N-CC/DTT-AuNCs system. (C) Zeta potentials of CC/DTT-AuNCs in the absence and presence of 10 μ M AQ4N. (D) Emission decay profiles of CC/DTT-AuNCs and CC/DTT-AuNCs + 1 μ M AQ4N.

3.3. Optimizing the Test Conditions for AQ4N

The main operational parameters, including the solution pH, incubation time, and incubation temperature for the CC/DTT-AuNC-based AQ4N luminescent sensing system, were examined. The value of ΔF ($\Delta F = F_0 - F$, where F_0 and F are the luminescence intensities of CC/DTT-AuNCs at 645 nm before and after the addition of AQ4N, respectively) was calculated and used to evaluate the quenching ability of AQ4N. The influence of solution pH on the AQ4N detection assay was tested by varying the phosphate buffer pH from 5.5 to 10, and the results displayed that the maximum ΔF appeared at pH 6.0 (Figure 3A). Therefore, a pH 6.0 solution was chosen in the subsequent experiments. The time-dependent curve manifested that the luminescence response of CC/DTT-AuNCs toward AQ4N is quite rapid, which can be finished within 30 s (Figure 3B). Hence, PL intensities of the reaction solutions were recorded immediately. Finally, we tested the influence of the incubation temperature on the AQ4N sensing system, and the results showed that ΔF reaches a maximum value at 25 $^{\circ}$ C and decreases with a further increase in temperature. The decreasing ΔF value at higher temperatures is reasonably owed to the weak electronic wavefunction coupling of the reactants according to a classical theory [11]. Thus, we conducted the follow-up experiments at 25 $^{\circ}$ C.

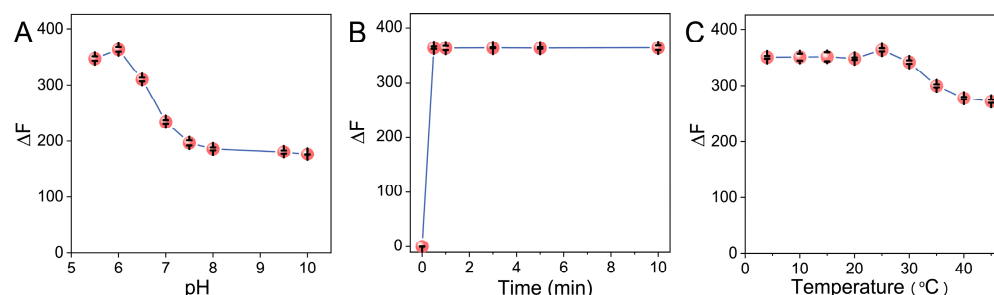


Figure 3. Influences of (A) solution pH, (B) incubation time, and (C) incubation temperature on the proposed AQ4N sensing system. The concentration of AQ4N is 0.5 μM .

3.4. Sensing Performance

To ensure that this method will exhibit satisfied sensitivity, the optimal conditions (pH 6.0 and 25 $^{\circ}\text{C}$) were employed to assess the performance of a CC/DTT-AuNC-based PET sensor toward AQ4N detection. As displayed in Figure 4A, the PL intensity of the CC/DTT-AuNCs decreased gradually with increasing AQ4N concentrations. A good linear relationship ($\Delta F = 1.3[\text{AQ4N}] + 32.4$; [AQ4N]: nM; $r = 0.997$) emerges between the ΔF value and the AQ4N concentration over the range of 25–200 nM (Figure 4B). The limit of detection (LOD) was calculated to be as low as 5 nM (based on $3\sigma/S$, where σ and S are the standard deviation of blank signals and slope of the working curve, respectively), which is obviously lower than the reported HPLC method [5]. A 1.7% relative standard deviation (RSD) was obtained for six parallel tests ([AQ4N] = 150 nM), suggesting the high reproducibility of the proposed assay system.

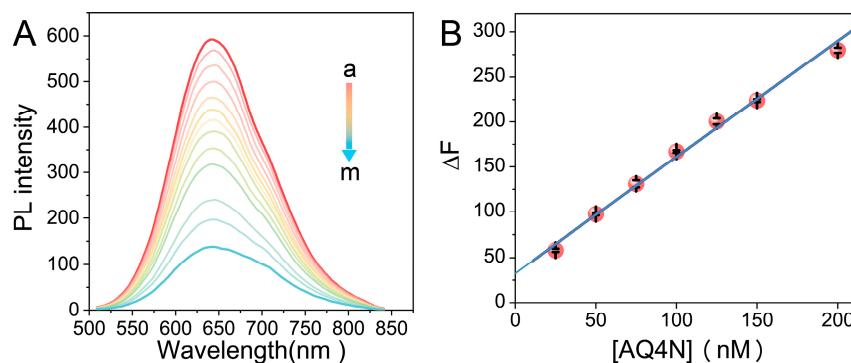


Figure 4. (A) The photoemission spectra of CC/DTT-AuNCs in the presence of various amounts of AQ4N. From a to m: 0, 25, 50, 75, 100, 125, 150, 175, 200, 250, 400, 500, and 750 nM. (B) ΔF as a function of AQ4N concentration.

To validate the specificity of the developed method, potential interfering agents were added to this AQ4N determination system. It can be clearly seen from Figure 5 that only AQ4N can induce a notable change for CC/DTT-AuNC luminescence, demonstrating the high specificity of this approach.

3.5. Detection of AQ4N in Real Samples

Due to the dose-related toxicity of AQ4N, it is necessary to monitor the blood AQ4N concentration during clinical applications. The feasibility of the constructed PET sensor was testified by analyzing the concentration of AQ4N in mouse plasma samples. The detection results were summarized in Table 1, wherein the AQ4N concentrations were determined by our proposed approach and the HPLC method, respectively. A *t*-test and an *F*-test conducted at a confidence level of 95% revealed that there were no significant differences in the values measured by using the two methods. These results confirmed that this fluorometric assay is appropriate for the quantification of AQ4N in real samples.

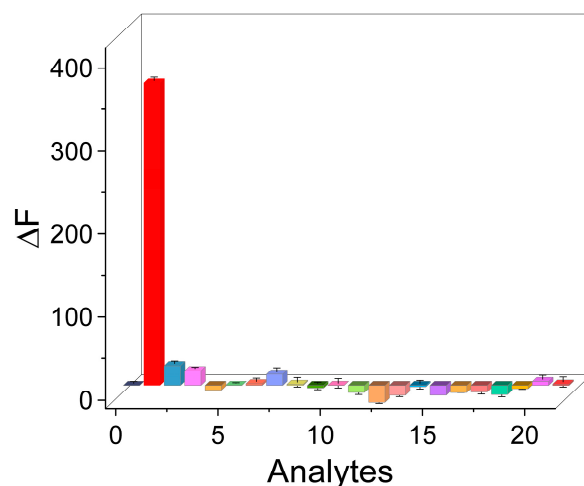


Figure 5. Specificity of the developed detection method for AQ4N. The labels of number marked on the X-axis correspond to (0) blank, (1) AQ4N, (2) Fe^{2+} , (3) Fe^{3+} , (4) Zn^{2+} , (5) Mg^{2+} , (6) K^+ , (7) Na^+ , (8) HCO_3^- , (9) GSH, (10) His, (11) BSA, (12) Ca^{2+} , (13) NAC, (14) CAR, (15) AA, (16) glucose, (17) urea, (18) Cys, (19) DDP, (20) alizarin, and (21) rhein. The concentrations of AQ4N and BSA were set at $0.5 \mu\text{M}$ and $40 \mu\text{g/mL}$, respectively. The concentrations of alizarin and rhein were $1 \mu\text{M}$. The concentrations of other tested substances were $10 \mu\text{M}$.

Table 1. Detection of AQ4N in mouse plasma.

Sample	Our method (μM , Mean \pm SD, $n = 3$)	HPLC Method (μM , mean \pm SD, $n = 3$)	F-Test ^a	<i>t</i> -Test ^a
1	82.5 ± 1.2	78.2 ± 0.02	7.93	1.42
2	81.8 ± 0.6	78.3 ± 0.04	5.23	1.79
3	74.6 ± 1.9	78.4 ± 0.08	5.87	1.18

^a $F_{0.05,2,2} = 19.00$, $t_{0.05,4} = 2.776$.

4. Conclusions

In summary, relying on the molecule-like PET property of AuNCs, a new fluorescence-sensing strategy was developed for rapid, sensitive, and selective monitoring of AQ4N. Based on the results of energetic and optical studies, it was found that the significant luminescence quenching in AQ4N-CC/DTT-AuNCs complexes mainly stems from a Coulomb interaction-accelerated PET process. Compared with the frequently used HPLC method, the strategy demonstrated here not only possesses comparable reproducibility and feasibility but also averts the complicated processing steps and use of toxic organic solvents. We believe that this paper will promote further works on the fabrication and application of fluorescence PET sensors in drug discovery and clinical practice.

Supplementary Materials: The following supporting information can be downloaded at: <https://www.mdpi.com/article/10.3390/nano12111861/s1>, Figure S1: Cyclic voltammogram curve of CC/DTT-AuNCs; Figure S2: Cyclic voltammogram curve of AQ4N; Figure S3: UV-vis absorption spectrum of CC/DTT-AuNCs; Figure S4: The absorption spectrum of AQ4N; Figure S5: The AQ4N concentration-dependent quenching efficiency determined for the CC/DTT-AuNCs before and after correction by the IFE formula; Table S1: Screening of AuNCs candidate using PET theory; Table S2: IFE on the luminescence response of CC/DTT-AuNCs toward AQ4N. References [30,44–51] were cited in supplementary materials.

Author Contributions: Conceptualization, H.-H.D. and W.C.; Methodology, K.-Y.H. and W.-H.W.; Validation, K.-Y.H., W.-H.W. and X.H.; Investigation, H.-X.H. and H.A.A.N.; Writing—Original Draft Preparation, K.-Y.H.; Writing—Review and Editing, H.-H.D. and W.C.; Funding Acquisition, H.-H.D. and W.C. All authors have read and agreed to the published version of the manuscript.

Funding: The authors gratefully acknowledge financial support of the National Natural Science Foundation of China (nos. 21675024 and 21804021), the Program for Innovative Leading Talents in Fujian Province (no. 2016B016), the Program for Innovative Research Team in Science and Technology in Fujian Province University (no. 2018B033), the Natural Science Foundation of Fujian Province (no. 2019J01304).

Data Availability Statement: The data presented in this study are available on request from the corresponding author.

Conflicts of Interest: The authors declare no conflict of interest.

References

1. Patterson, L.H.; McKeown, S.R. AQ4N: A New Approach to Hypoxia-Activated Cancer Chemotherapy. *Br. J. Cancer* **2000**, *83*, 1589–1593. [[CrossRef](#)] [[PubMed](#)]
2. Albertella, M.R.; Loadman, P.M.; Jones, P.H.; Phillips, R.M.; Rampling, R.; Burnet, N.; Alcock, C.; Anthoney, A.; Vjaters, E.; Dunk, C.R.; et al. Hypoxia-Selective Targeting by the Bioreductive Prodrug AQ4N in Patients with Solid Tumors: Results of a Phase I Study. *Clin. Cancer Res.* **2008**, *14*, 1096–1104. [[CrossRef](#)] [[PubMed](#)]
3. Shao, F.; Wu, Y.; Tian, Z.; Liu, S. Biomimetic Nanoreactor for Targeted Cancer Starvation Therapy and Cascade Amplified Chemotherapy. *Biomaterials* **2021**, *274*, 120869. [[CrossRef](#)] [[PubMed](#)]
4. Shen, S.; Wu, Y.; Li, K.; Wang, Y.; Wu, J.; Zeng, Y.; Wu, D. Versatile Hyaluronic Acid Modified AQ4N-Cu(II)-Gossypol Infinite Coordination Polymer Nanoparticles: Multiple Tumor Targeting, Highly Efficient Synergistic Chemotherapy, and Real-Time Self-Monitoring. *Biomaterials* **2018**, *154*, 197–212. [[CrossRef](#)] [[PubMed](#)]
5. Swaine, D.J.; Loadman, P.M.; Bibby, M.C.; Graham, M.A.; Patterson, L.H. High-Performance Liquid Chromatographic Analysis of AQ4N, an Alkylaminoanthraquinone N-Oxide. *J. Chromatogr. B* **2000**, *742*, 239–245. [[CrossRef](#)]
6. Atkinson, S.J.; Loadman, P.M.; Sutton, C.; Patterson, L.H.; Clench, M.R. Examination of the Distribution of the Bioreductive Drug AQ4N and Its Active Metabolite AQ4 in Solid Tumours by Imaging Matrix-Assisted Laser Desorption/Ionisation Mass Spectrometry. *Rapid Commun. Mass Spectrom.* **2007**, *21*, 1271–1276. [[CrossRef](#)]
7. Daly, B.; Ling, J.; de Silva, A.P. Current Developments in Fluorescent PET (Photoinduced Electron Transfer) Sensors and Switches. *Chem. Soc. Rev.* **2015**, *44*, 4203–4211. [[CrossRef](#)]
8. Sun, W.; Li, M.; Fan, J.; Peng, X. Activity-Based Sensing and Theranostic Probes Based on Photoinduced Electron Transfer. *Acc. Chem. Res.* **2019**, *52*, 2818–2831. [[CrossRef](#)]
9. Escudero, D. Revising Intramolecular Photoinduced Electron Transfer (PET) from First-Principles. *Acc. Chem. Res.* **2016**, *49*, 1816–1824. [[CrossRef](#)]
10. Chi, W.; Chen, J.; Liu, W.; Wang, C.; Qi, Q.; Qiao, Q.; Tan, T.M.; Xiong, K.; Liu, X.; Kang, K.; et al. A General Descriptor ΔE Enables the Quantitative Development of Luminescent Materials Based on Photoinduced Electron Transfer. *J. Am. Chem. Soc.* **2020**, *142*, 6777–6785. [[CrossRef](#)]
11. Marcus, R.A. Electron Transfer Reactions in Chemistry. Theory and Experiment. *Rev. Mod. Phys.* **1993**, *65*, 599–610. [[CrossRef](#)]
12. Wang, S.; Sun, J.; Zhao, J.; Lu, S.; Yang, X. Photo-Induced Electron Transfer-Based Versatile Platform with G-Quadruplex/Hemin Complex as Quencher for Construction of DNA Logic Circuits. *Anal. Chem.* **2018**, *90*, 3437–3442. [[CrossRef](#)] [[PubMed](#)]
13. Zhang, L.; Zhu, J.; Guo, S.; Li, T.; Li, J.; Wang, E. Photoinduced Electron Transfer of DNA/Ag Nanoclusters Modulated by G-Quadruplex/Hemin Complex for the Construction of Versatile Biosensors. *J. Am. Chem. Soc.* **2013**, *135*, 2403–2406. [[CrossRef](#)] [[PubMed](#)]
14. Pantazis, A.; Westerberg, K.; Althoff, T.; Abramson, J.; Olcese, R. Harnessing Photoinduced Electron Transfer to Optically Determine Protein Sub-Nanoscale Atomic Distances. *Nat. Commun.* **2018**, *9*, 4738. [[CrossRef](#)] [[PubMed](#)]
15. Wang, G.; Zhu, Y.; Chen, L.; Zhang, X. Photoinduced Electron Transfer (PET) Based Label-Free Aptasensor for Platelet-Derived Growth Factor-Bb and Its Logic Gate Application. *Biosens. Bioelectron.* **2015**, *63*, 552–557. [[CrossRef](#)]
16. Nawimanager, R.R.; Prasai, B.; Hettiarachchi, S.U.; McCarley, R.L. Rapid, Photoinduced Electron Transfer-Modulated, Turn-on Fluorescent Probe for Detection and Cellular Imaging of Biologically Significant Thiols. *Anal. Chem.* **2014**, *86*, 12266–12271. [[CrossRef](#)]
17. Dong, B.; Lu, Y.; Zhang, N.; Song, W.; Lin, W. Ratiometric Imaging of Cysteine Level Changes in Endoplasmic Reticulum during H₂O₂-Induced Redox Imbalance. *Anal. Chem.* **2019**, *91*, 5513–5516. [[CrossRef](#)]
18. Tang, Y.; Gu, C.; Wang, C.; Song, B.; Zhou, X.; Lou, X.; He, M. Evanescent Wave Aptasensor for Continuous and Online Aminoglycoside Antibiotics Detection Based on Target Binding Facilitated Fluorescence Quenching. *Biosens. Bioelectron.* **2018**, *102*, 646–651. [[CrossRef](#)]
19. Tang, Y.; Gu, C.; Wang, C.; Song, B.; Zhou, X.; Lou, X.; He, M. Highly Water-Stable Dye@Ln-MOFs for Sensitive and Selective Detection toward Antibiotics in Water. *ACS Appl. Mater. Interfaces* **2019**, *11*, 21201–21210.
20. Dwivedi, S.K.; Gupta, R.C.; Srivastava, P.; Singh, P.; Koch, B.; Maiti, B.; Misra, A. Dual Fluorophore Containing Efficient Photoinduced Electron Transfer Based Molecular Probe for Selective Detection of Cr³⁺ and PO₄³⁻ Ions through Fluorescence “Turn-On–Off” Response in Partial Aqueous and Biological Medium: Live Cell Imaging and Logic Application. *Anal. Chem.* **2018**, *90*, 10974–10981.

21. Uchiyama, S.; Fukatsu, E.; McClean, G.D.; de Silva, A.P. Measurement of Local Sodium Ion Levels near Micelle Surfaces with Fluorescent Photoinduced-Electron-Transfer Sensors. *Angew. Chem. Int. Ed.* **2016**, *55*, 768–771. [[CrossRef](#)] [[PubMed](#)]
22. Cao, Y.; Malola, S.; Matus, M.F.; Chen, T.; Yao, Q.; Shi, R.; Häkkinen, H.; Xie, J. Reversible Isomerization of Metal Nanoclusters Induced by Intermolecular Interaction. *Chem* **2021**, *7*, 2227–2244. [[CrossRef](#)]
23. Wu, Z.; Du, Y.; Liu, J.; Yao, Q.; Chen, T.; Cao, Y.; Zhang, H.; Xie, J. Auophilic Interactions in the Self-Assembly of Gold Nanoclusters into Nanoribbons with Enhanced Luminescence. *Angew. Chem. Int. Ed.* **2019**, *58*, 8139–8144. [[CrossRef](#)] [[PubMed](#)]
24. Qian, S.; Wang, Z.; Zuo, Z.; Wang, X.; Wang, Q.; Yuan, X. Engineering Luminescent Metal Nanoclusters for Sensing Applications. *Coord. Chem. Rev.* **2022**, *451*, 214268. [[CrossRef](#)]
25. Li, Q.; Zhou, M.; So, W.Y.; Huang, J.; Li, M.; Kauffman, D.R.; Cotlet, M.; Higaki, T.; Peteanu, L.A.; Shao, Z.; et al. A Mono-Cuboctahedral Series of Gold Nanoclusters: Photoluminescence Origin, Large Enhancement, Wide Tunability, and Structure–Property Correlation. *J. Am. Chem. Soc.* **2019**, *141*, 5314–5325. [[CrossRef](#)]
26. Shang, L.; Xu, J.; Nienhaus, G.U. Recent Advances in Synthesizing Metal Nanocluster-Based Nanocomposites for Application in Sensing, Imaging and Catalysis. *Nano Today* **2019**, *28*, 100767. [[CrossRef](#)]
27. Kwak, K.; Lee, D. Electrochemistry of Atomically Precise Metal Nanoclusters. *Acc. Chem. Res.* **2019**, *52*, 12–22. [[CrossRef](#)]
28. Zhou, M.; Du, X.; Wang, H.; Jin, R. The Critical Number of Gold Atoms for a Metallic State Nanocluster: Resolving a Decades-Long Question. *ACS Nano* **2021**, *15*, 13980–13992. [[CrossRef](#)]
29. Zhou, G.; Lu, G.; Prezhdo, O.V. Modeling Auger Processes with Nonadiabatic Molecular Dynamics. *Nano Lett.* **2021**, *21*, 756–761. [[CrossRef](#)]
30. Huang, K.; Fang, Q.; Sun, W.; He, S.; Yao, Q.; Xie, J.; Chen, W.; Deng, H. Cucurbit[n]uril Supramolecular Assemblies-Regulated Charge Transfer for Luminescence Switching of Gold Nanoclusters. *J. Phys. Chem. Lett.* **2022**, *13*, 419–426. [[CrossRef](#)]
31. Deng, H.H.; Huang, K.Y.; Zhu, C.T.; Shen, J.F.; Zhang, X.P.; Peng, H.P.; Xia, X.H.; Chen, W. Bell-Shaped Electron Transfer Kinetics in Gold Nanoclusters. *J. Phys. Chem. Lett.* **2021**, *12*, 876–883. [[CrossRef](#)] [[PubMed](#)]
32. Stamplecoskie, K.G.; Kamat, P.V. Size-Dependent Excited State Behavior of Glutathione-Capped Gold Clusters and Their Light-Harvesting Capacity. *J. Am. Chem. Soc.* **2014**, *136*, 11093–11099. [[CrossRef](#)] [[PubMed](#)]
33. Stamplecoskie, K.G.; Chen, Y.S.; Kamat, P.V. Excited-State Behavior of Luminescent Glutathione-Protected Gold Clusters. *J. Phys. Chem. C* **2014**, *118*, 1370–1376. [[CrossRef](#)]
34. Kato, D.; Sakai, H.; Saegusa, T.; Tkachenko, N.V.; Hasobe, T. Synthesis, Structural and Photophysical Properties of Pentacene Alkanethiolate Monolayer-Protected Gold Nanoclusters and Nanorods: Supramolecular Intercalation and Photoinduced Electron Transfer with C₆₀. *J. Phys. Chem. C* **2017**, *121*, 9043–9052. [[CrossRef](#)]
35. Huang, K.Y.; He, H.X.; He, S.B.; Zhang, X.P.; Peng, H.P.; Lin, Z.; Deng, H.H.; Xia, X.H.; Chen, W. Gold Nanocluster-Based Fluorescence Turn-off Probe for Sensing of Doxorubicin by Photoinduced Electron Transfer. *Sens. Actuators B* **2019**, *296*, 126656. [[CrossRef](#)]
36. Chen, S.; Yu, Y.L.; Wang, J.H. Inner Filter Effect-Based Fluorescent Sensing Systems: A Review. *Anal. Chim. Acta* **2018**, *999*, 13–26. [[CrossRef](#)]
37. Farid, S.; Dinnocenzo, J.P.; Merkel, P.B.; Young, R.H.; Shukla, D.; Guirado, G. Reexamination of the Rehm–Weller Data Set Reveals Electron Transfer Quenching That Follows a Sandros–Boltzmann Dependence on Free Energy. *J. Am. Chem. Soc.* **2011**, *133*, 11580–11587. [[CrossRef](#)]
38. Fu, Y.; Cen, D.; Zhang, T.; Jiang, S.; Wang, Y.; Cai, X.; Li, X.; Han, G. Implantable Fibrous Scaffold with Hierarchical Microstructure for the ‘On-Site’ Synergistic Cancer Therapy. *Chem. Eng. J.* **2020**, *402*, 126204. [[CrossRef](#)]
39. Rosenberg, M.; Junker, A.K.R.; Sørensen, T.J.; Laursen, B.W. Fluorescence pH Probes Based on Photoinduced Electron Transfer Quenching of Long Fluorescence Lifetime Triangulenium Dyes. *ChemPhotoChem* **2019**, *3*, 233–242. [[CrossRef](#)]
40. Wehlin, S.A.M.; Troian Gautier, L.; Li, G.; Meyer, G.J. Chloride Oxidation by Ruthenium Excited-States in Solution. *J. Am. Chem. Soc.* **2017**, *139*, 12903–12906. [[CrossRef](#)]
41. Kavarnos, G.J.; Turro, N.J. Photosensitization by Reversible Electron Transfer: Theories, Experimental Evidence, and Examples. *Chem. Rev.* **1986**, *86*, 401–449. [[CrossRef](#)]
42. Kovacs, D.; Mathieu, E.; Kiraev, S.R.; Wells, J.A.L.; Demeyere, E.; Sipos, A.; Borbas, K.E. Coordination Environment-Controlled Photoinduced Electron Transfer Quenching in Luminescent Europium Complexes. *J. Am. Chem. Soc.* **2020**, *142*, 13190–13200. [[CrossRef](#)] [[PubMed](#)]
43. Deng, H.H.; Huang, K.Y.; He, S.B.; Xue, L.P.; Peng, H.P.; Zha, D.J.; Sun, W.M.; Xia, X.H.; Chen, W. Rational Design of High-Performance Donor–Linker–Acceptor Hybrids Using a Schiff Base for Enabling Photoinduced Electron Transfer. *Anal. Chem.* **2020**, *92*, 2019–2026. [[CrossRef](#)] [[PubMed](#)]
44. Xiu, L.F.; Huang, K.Y.; Zhu, C.T.; Zhang, Q.; Peng, H.P.; Xia, X.H.; Chen, W.; Deng, H.H. Rare-Earth Eu³⁺/Gold Nanocluster Ensemble-Based Fluorescent Photoinduced Electron Transfer Sensor for Biomarker Dipicolinic Acid Detection. *Langmuir* **2021**, *37*, 949–956. [[CrossRef](#)]
45. Deng, H.H.; Zhang, L.N.; He, S.B.; Liu, A.L.; Li, G.W.; Lin, X.H.; Xia, X.H.; Chen, W. Methionine-Directed Fabrication of Gold Nanoclusters with Yellow Fluorescent Emission for Cu²⁺ Sensing. *Biosens. Bioelectron.* **2015**, *65*, 397–403. [[CrossRef](#)]
46. Peng, H.; Jian, M.; Deng, H.; Wang, W.; Huang, Z.; Huang, K.; Liu, A.; Chen, W. Valence States Effect on Electrogenerated Chemiluminescence of Gold Nanocluster. *ACS Appl. Mater. Interfaces* **2017**, *9*, 14929–14934. [[CrossRef](#)]

47. Deng, H.H.; Wu, G.W.; Zou, Z.Q.; Peng, H.P.; Liu, A.L.; Lin, X.H.; Xia, X.H.; Chen, W. pH-Sensitive Gold Nanoclusters: Preparation and Analytical Applications for Urea, Urease, and Urease Inhibitor Detection. *Chem. Commun.* **2015**, *51*, 7847–7850. [[CrossRef](#)]
48. Sun, J.; Yue, Y.; Wang, P.; He, H.; Jin, Y. Facile and Rapid Synthesis of Water-Soluble Fluorescent Gold Nanoclusters for Sensitive and Selective Detection of Ag⁺. *J. Mater. Chem. C* **2013**, *1*, 908–913. [[CrossRef](#)]
49. Sun, J.; Wu, H.; Jin, Y. Synthesis of Thiolated Ag/Au Bimetallic Nanoclusters Exhibiting an Anti-Galvanic Reduction Mechanism and Composition-Dependent Fluorescence. *Nanoscale* **2014**, *6*, 5449–5457. [[CrossRef](#)]
50. Tang, Y.; Xu, J.; Xiong, C.; Xiao, Y.; Zhang, X.; Wang, S. Enhanced Electrochemiluminescence of Gold Nanoclusters via Silver Doping and Their Application for Ultrasensitive Detection of Dopamine. *Analyst* **2019**, *144*, 2643–2648. [[CrossRef](#)]
51. Luo, Z.; Yuan, X.; Yu, Y.; Zhang, Q.; Leong, D.T.; Lee, J.Y.; Xie, J. From Aggregation-Induced Emission of Au(I)-Thiolate Complexes to Ultrabright Au(0)@Au(I)-Thiolate Core-Shell Nanoclusters. *J. Am. Chem. Soc.* **2012**, *134*, 16662–16670. [[CrossRef](#)] [[PubMed](#)]